# Lawrence Berkeley National Laboratory

## Lawrence Berkeley National Laboratory

### Title

Structural Changes in the Mn4Ca Cluster and the Mechanism of Photosynthetic Water Splitting

### Permalink

https://escholarship.org/uc/item/3gk2g325

### Author

Pushkar, Y.

### Publication Date

2008-02-01

Peer reviewed

eScholarship.org Powered by the California Digital Library
University of California

Biophysics

# Structural Changes in the $Mn_4Ca$ Cluster and the Mechanism of Photosynthetic Water Splitting

Yulia Pushkar,[1,2] Junko Yano,[1,2]‡ Kenneth Sauer,[1,2]

Alain Boussac,[3]‡ Vittal K. Yachandra[1]‡

[1]Melvin Calvin Laboratory, Physical Biosciences Division, Lawrence Berkeley National Laboratory, Berkeley, CA 94720-5230, USA

[2]Department of Chemistry, University of California, Berkeley, CA 94720-5230, USA

[3]CEA, URA CNRS 2096, Saclay, 91191 Gif sur Yvette, Cedex, France

‡To whom correspondence should be addressed. e-mail: jyano@lbl.gov (J.Y.); alain.boussac@cea.fr (A.B); vkyachandra@lbl.gov (V.K.Y)

**Abstract**

Photosynthetic water oxidation, where water is oxidized to dioxygen, is a fundamental chemical reaction that sustains the biosphere. This reaction is catalyzed by a $Mn_4Ca$ complex in the Photosystem II (PS II) oxygen-evolving complex (OEC); a multi-protein assembly embedded in the thylakoid membranes of green plants, cyanobacteria and algae. The mechanism of photosynthetic water oxidation by the $Mn_4Ca$ cluster in photosystem II is the subject of much debate although lacking structural characterization of the catalytic intermediates. Biosynthetically exchanged Ca/Sr-PS II preparations, and x-ray spectroscopy including Extended X-ray Absorption Fine Structure (EXAFS) allowed us to monitor Mn-Mn and Ca(Sr)-Mn distances in the four intermediate S-states, $S_0$ through $S_3$, of the catalytic cycle, which couples the one-electron photochemistry occurring at the PS II reaction center with the four-electron water oxidation chemistry taking place at the $Mn_4Ca(Sr)$ cluster. We have detected significant changes in the structure of the complex; especially, in the Mn-Mn and Ca(Sr)-Mn distances upon the $S_2$ to $S_3$ and $S_3$ to $S_0$ transitions. These results implicate the involvement of at least one common bridging oxygen atom between the Mn-Mn and Mn-Ca(Sr) atoms in the O-O bond formation. Since PS II cannot advance beyond the $S_2$ state in preparations that lack Ca(Sr), these results show that Ca(Sr) is one of the critical requirements for the mechanism of the enzyme. The results also show that Ca is not just a spectator atom involved in providing a structural framework but is actively involved in the mechanism of water oxidation and represents a rare example of a catalytically active Ca cofactor.

Photosynthetic water oxidation, where water is oxidized to dioxygen is catalyzed by a $Mn_4Ca$ complex in the oxygen-evolving complex (OEC) of Photosystem II (PS II) (1, 2); a multi-protein assembly embedded in the thylakoid membranes of green plants, cyanobacteria and algae. The structure and function of the $Mn_4Ca$ cluster, the heart of the OEC, has been under active investigation by many spectroscopic techniques such as EPR/ENDOR (3-7), x-ray spectroscopy (8-10) and FTIR (11, 12). X-ray diffraction (XRD) studies at 3.0 - 3.8 Å resolution have located the $Mn_4Ca$ cluster in the electron-density map and confirmed the presence of Ca in the OEC cluster (13, 14), that was first detected using Ca and Sr x-ray spectroscopy (XAS) studies (15-19). Mn-, Ca- and Sr-EXAFS (extended x-ray absorption fine structure) studies of PS II frozen solutions have provided accurate distances (~0.02 Å) and the numbers of Mn-Mn, Mn-Ca and Mn/Ca-ligand vectors in the $Mn_4Ca$ cluster (8, 20). XAS experiments require a significantly lower x-ray dose than XRD measurements, and the onset of radiation damage can be precisely determined and controlled by monitoring the Mn K-edge position, thus allowing us to collect data from the intact $Mn_4Ca$ cluster of PS II. Recently, a high-resolution $Mn_4Ca$ structural model was determined using a polarised Mn-EXAFS study on PS II single crystals in the $S_1$ state (21). Of all the cations that can competitively replace Ca in PS II, only Sr is capable of supporting $O_2$ evolution, a feature that has been attributed to the similar electronegativities of Ca and Sr and, hence, to their similar Lewis acidities and pKa values of water ligands (22, 23). Substituting Sr for Ca alters the EPR properties of the $S_2$ state, increasing the fraction of PS II that exhibit a $g \approx 4.1$ or $g \approx 5.25$ EPR signal and altering the appearance of the g=2 multiline EPR signal (22, 24, 25). Presence Sr also shifts a low-frequency $S_2$ state vibrational mode that has been assigned to a Mn-O-Mn

structural unit (26) as well as alters several carboxylate stretching modes of the $S_2$-minus-$S_1$ FTIR difference spectrum (27, 28). This demonstrates that Ca substitution for Sr only slightly perturbs the structure of $Mn_4$ cluster making Sr a relevant spectroscopic probe.

This x-ray absorption study determines the changes in the Mn-Mn and Ca(Sr)-Mn distances in the four intermediate S-states, $S_0$ through $S_3$, of the catalytic cycle, which couples the one-electron photochemistry occurring at the PS II reaction center with the four-electron water oxidation chemistry taking place at the $Mn_4Ca$ cluster (2). This became possible by the use of unique PS II preparations from the thermophilic cyanobacterium, *Thermosynechococcus elongatus*, with Ca biosynthetically replaced by isomorphous Sr (29). The advantages over Ca/Sr exchange by biochemical procedures are: i) an enzyme fully competent in $O_2$ evolution, ii) a 1:1 Sr to PS II ratio monitored by Sr quantitation, and iii) EXAFS measurements at the Sr K-edge compared to those at the lower-energy Ca K-edge are less prone to x-ray damage and are preferred for experimental reasons (17-19).

## Results

### EPR spectroscopic quantitation of S-state composition

Protein samples in the $S_1$ state were advanced to primarily $S_2$, $S_3$ and $S_0$ states by giving 1, 2 and 3 laser flashes followed by immediate freezing in liquid nitrogen. Starting from dark adapted, the $S_2$-state multiline EPR signal is maximal after 1 flash and oscillates with a period of four as a function of flash number; thus, the $S_2$-state multiline EPR signal can be used to characterize the S-state distribution of samples given 0, 1, 2, 3, 4, 5 or 6 flashes. Fig. S1A shows typical EPR spectra obtained after a given flash number. A deep period-four oscillation is observed with maxima on the first and fifth

flashes, indicating that there is very little dephasing of S-state advancement with flashes and an initial S-state population close to 100% $S_1TyrD_{ox}$. The S-state composition of each sample was determined by EPR (Fig. S1, Tables 1, 2), and these data were used to generate the x-ray spectra of the pure S-states.

**X-ray absorption spectroscopy at the Mn K-edge**

Mn XANES and EXAFS data were collected for all S-state samples ensuring the integrity of the samples and the absence of radiation damage to the structure of the $Mn_4$ core (Fig. 1). The resulting Mn spectra were similar to those from the same S-states in Ca containing PS II protein complexes isolated from spinach (30, 31) or the thermophilic cyanobacterium (21, 32). The edge shift that is apparent between the $S_1$ and $S_2$ spectra (Fig. 1A) indicates that Mn oxidation occurs during the $S_1$ to $S_2$ transition. However, it is less clear that there is a shift between the $S_2$ and $S_3$ spectra, which suggests that Mn is not oxidized as the OEC proceeds from the $S_2$ to $S_3$ state. The edge position shifts to lower energy between the $S_3$ and $S_0$ spectra as expected for $S_3 \rightarrow [S_4] \rightarrow S_0$ transition.

In Fourier transform (FT) of the Mn EXAFS data (Fig. 1B), FT peak I is characteristic of the 1.8 Å Mn-oxo bridging ligand distances, FT peak II is best fit to two to three di-μ-oxo bridged Mn-Mn interaction at ~2.7 Å (Table 3), and FT peak III is from one mono-μ-oxo bridged Mn-Mn and Mn-Sr interactions. The presence of these three Fourier peaks is a requisite marker for the presence of an intact bridged multinuclear $Mn_4Ca(Sr)$ complex., The $Mn_4Sr$ and $Mn_4Ca$ clusters are essentially identical in the structure of $Mn_4$-core and this is not surprising, because these clusters exhibit only small differences in their kinetic and spectroscopic properties. Detailed analysis and

comparison of the Sr-containing PS II samples with Ca-containing PS II samples is underway and will be published elsewhere.

Mn EXAFS of the $S_1$, $S_2$ and $S_0$ states are similar, however, as Fig. 1B shows $S_3$ state spectrum differs from all other S-states. In the $S_3$ state the intensity of FT peak II decreases and peak III appears to be almost smeared out. This can only be explained by changes in Mn-Mn and Mn-Sr distances and thus by structural changes in OEC upon the $S_2$ to $S_3$ and $S_3 \rightarrow [S_4] \rightarrow S_0$ transitions (Table 3). The low intensity of FT peak III (there are 4 Mn/1Sr) prevents reliable analysis of Mn-Sr interaction from the 'Mn' point of view, however, as demonstrated below, the Sr EXAFS technique can clearly resolve the Sr-Mn interaction from the 'Sr' point of view in all the S-states..

**X-ray absorption spectroscopy at the Sr K-edge**

The Sr K-edge x-ray near-edge spectra (XANES) of Sr-PS II, which corresponds to dipole-allowed transitions from the 1s core level to molecular orbitals with predominant p character, contain information about the valence and coordination environment of the absorbing atom. The Sr XANES spectra of Sr-PS II show that there is a pronounced difference between the S-state spectra and the spectrum of *inactive* Sr-PS II after the $Mn_4Sr$ cluster is disrupted by hydroxylamine (HYD) (Fig. 2A). This shows that in active PS II the Sr first coordination environment is different from that of free $Sr^{2+}$ ion. Moreover, there are differences in the Sr XANES in the $S_1$, $S_2$, $S_3$ and $S_0$ states indicating that Sr(Ca) is an integral part of the cluster, thus sensitive to changes in the electronic structure, as the cluster cycles through the S-states, caused by changes in the oxidation state and geometry of the cluster.

The structural changes of the S-states are even more obvious in the Fourier transforms (FT) of the EXAFS spectra (Fig. 2B) of Sr-PS II in the $S_1$, $S_2$, $S_3$, $S_0$ states and the *inactive* control sample (HYD). Two major Fourier peaks, I and II, represent the radial distribution of the x-ray photoelectron backscattering from the atoms surrounding Sr. Fourier peak I is best simulated by one shell of 7 to 8 oxygen atoms at ~2.5 Å (Table S3). Fourier peak II consists of at least two different Sr-Mn interactions at ~3.5 Å and ~4.0 Å in all S-states (Table 4). This Fourier peak is absent in the inactive control sample (HYD), as there are no Sr-Mn interactions in this sample. Relative to the $S_1$ state sample, FT peak II is broadened in $S_2$ and split in the $S_3$ and $S_0$ states; these changes are significant.

## Discussion

### Position of Sr atom in the OEC in the $S_1$ state

Previously, the Ca EXAFS of the native PS II (18) and Sr EXAFS on Sr-reactivated PS II membranes (17) indicated proximity of the Ca at 3.4 Å and Sr at 3.5 Å to the Mn-cluster in the $S_1$ dark-stable state of the OEC. The present study unambiguously demonstrates Sr to be proximate to the OEC in all S-states, and that significant changes occur in the Sr(Ca)-Mn interactions as the enzyme proceeds through the catalytic cycle, as seen in the FTs in Fig. 2B and Table 4. The Sr-Mn distances in the recently reported first heteronuclear Mn/Sr complex (33), where Mn and Sr are bridged by an oxo group, are similar to those observed in PS II. Therefore, it is likely that the Ca/Sr atom in PS II is bridged by a μ-oxo group to Mn atoms.

The best fits (Table 4) to the Sr EXAFS data (Fig. 2B) in the $S_0$ through $S_3$ states are obtained for Sr-Mn distances at a short ~3.5 Å and a long ~ 4.0 Å. The best fits for

the $S_1$ state are for 3:1, 2:2 and 2:1 short:long Sr-Mn distance ratio; however, the 3:1 fit is better than the others by as much as 25-28% (Table 4 and Fig. S4). The best fit for the $S_2$ state is for a 3:1 or 2:2 short to long Sr-Mn distance ratios, with the fit for 2:2 being better by 21%. For the $S_3$ and $S_0$ states, a ratio of 2:2 provides the best fit (Table 4 and Fig. S4). This information is used below to model the position of Sr and the important changes in the short and long Sr-Mn distances during the S-state transitions.

To model the position of the Sr atom in the $S_1$ state we combined information from the EXAFS fits (Table 4) and from polarized EXAFS measurements of Ca-containing PS II single crystals (21), from which three high-resolution $Mn_4Ca$ structural models (I, II, III) have been proposed (Fig. S5). For the three best fits (Table 4), there are 3 or 2 short Sr-Mn distances at ~3.5 Å and 1 or 2 Sr-Mn long distances at ~4.0 Å. For all three cases the Sr atom is displaced less than 1.2 Å from the position of Ca, and is directly connected to the Mn-core through a bridging oxygen atom. The Ca- and Sr-PS II are slightly different in their kinetic and spectroscopic properties (29) that may reflect differences in the interaction of Ca and Sr with the Mn atoms. Previous results from Ca EXAFS of plant PS II have shown that there are only 2 Mn-Ca distances (18) at <4 Å compared to the four we have observed in Sr-PS II; it is possible that the two longer interactions are at >4 Å or were not discernible at the S/N of the Ca EXAFS data (18). There is also evidence that Ca protects the accessibility to two of the four Mn atoms by reductants, suggesting a closer interaction between Ca and two of the four Mn atoms in the cluster (34). In Fig. 3A we use model II (from ref. 21) to illustrate the best possible position of the Sr atom (Fit 1 in Table 4, 3:1 ratio) in the $S_1$ state. The experimental FT from the $S_1$ state of Sr-PS II is comparable to the FT calculated for the structure shown in

Fig. 3B. Models I and III from Yano *et al*. (21) were also considered. Positions of Mn atoms in model III from Yano *et al*. (21) are identical to those in model II, resulting in the same Sr positions relative to the $Mn_4$ core (not shown). The Sr/Ca atom in model III is ~4 Å away from the $\mu_3$-oxo-bridged oxygen, requiring two additional μ-oxo bridges between Sr and Mn to explain the presence of two short distances. Range extended Mn EXAFS (35) results from oriented PS II membranes show that model I is less probable.

**Structural changes in the OEC**

Previous Mn-EXAFS experiments demonstrated the absence of major changes in Mn-Mn distances of the $Mn_4$-core during the $S_1$ to $S_2$ transition. Our present Mn and Sr-EXAFS data (Fig. 1B, 2B and Tables 3, 4) also show that there are no significant changes in the Mn-Mn and Sr-Mn distances during this transition. It is possible that the number of short:long Sr-Mn distance ratio changes from 3:1 ($S_1$) to 2:2 ($S_2$), on the basis of the quality of the fits (Table 4), indicating that one Sr-Mn distance changes from ~3.5 to ~4.0 Å during this transition. However, we cannot rule out the presence of the 2:2 ratio in the $S_1$ state or the 3:1 ratio in the $S_2$ state because of the uncertainties in EXAFS fitting procedures.

One shell fit of the peak II in Mn EXAFS of the $S_3$ state (Table 3) shows an elongation of the Mn-Mn distance as well as increased Debye-Waller factor as compared to $S_1$ and $S_2$ states. Introduction of the second Mn-Mn subshell improves fit quality and resolves two distances (2.75 Å and 2.88 Å) among di-μ-oxo bridged Mn-Mn units. Low intensity of the peak III prevents reliable analysis of the changes in the mono-μ-oxo bridged Mn-Mn and Mn-Sr interaction around 3.2-3.5 Å from Mn EXAFS.

The FT peak II in Sr EXAFS splits in the $S_3$ state (Fig. 2B) suggesting changes in Sr-Mn distances. The best fit (Table 4) for the $S_3$ state is for 2 short and 2 long Sr-Mn distances. The Sr-Mn interaction at ~3.5 Å shortens to ~3.4 Å, and the distance at ~4.0 Å decreases to ~3.9 Å during the $S_2$ to $S_3$ transition. The fact that Mn-Sr interactions change during the $S_2$ to $S_3$ transition is also in agreement with the different efficiency of Ca-depletion in the $S_3$-state from that in other S-states (36). Ca/Sr-depleted PS II cannot advance to the $S_3$ state; instead, a state designated $S_2Y_Z^{\bullet}$ is formed, in which the $Mn_4$-core structure is close to that of the $S_2$ state and does not resemble the structure of the native $S_3$ state (16, 31). We propose that the single $\mu_3$-oxygen of the $Mn_4Ca$ structure is important for the formation of the $S_3$ state and that its properties are significantly altered in the absence of a coordinated Ca/Sr atom.

Completing the catalytic cycle in the $S_3$ to $S_0$ transition, the di-μ-oxo bridged Mn-Mn interactions demonstrate shortening (Table 3) and recovery of peak III intensity in Mn EXAFS (Fig 1B). From Sr EXAFS, we can see that the two Sr-Mn distances at 3.42 Å and two at 3.94 Å increase to 3.47 Å and 3.98 Å respectively.During the $S_0$ to $S_1$ transition, the Sr-Mn distances return to ~3.5 Å and ~4.0 Å.

Fig. 4 summarizes the structural changes accompanying the $S_0$ to $S_3$ catalytic cycle transition as deduced from Mn and Sr EXAFS. Upon the oxidation of one Mn atom, probably $Mn_D$ (37, 38), during the $S_1$ to $S_2$ transition, it is possible that the Sr atom moves away from one Mn ($Mn_B$, $Mn_C$ or $Mn_D$) leading to the change from 3:1 short:long Sr-Mn distances to a 2:2 ratio in the $S_2$ state. Alternatively, the 2:2 ratio can be present already in the $S_1$ state (lower fit quality, Table 3) and, thus, remains unchanged in the $S_1$ to $S_2$ transition. During the $S_2$ to $S_3$ transition, although the ratio of short to long remains

2:2, there is a significant decrease in the Sr-Mn distances. From the Mn EXAFS the di-μ-oxo bridged Mn-Mn distances increase during the $S_2$ to $S_3$ transition; from ~2.7-2.8 Å to ~2.8-2.9 Å (Table 3). This result is similar to that detected by Mn-EXAFS using PS II preparations from spinach (31). Studies aiming on identifying which particular Mn-Mn unit in OEC model increases in distance are in progress.

**Mechanism of photosynthetic water oxidation**

It is hard to rationalize the changes in the Mn-Mn and Mn-Sr distances without significant involvement of the bridging O atoms. One hypothesis is that during the $S_2$ to $S_3$ transition the oxidation is predominantly from a bridging oxygen ligand triggering the structural changes in the OEC. A bridging ligand radical has been proposed on the basis of DFT calculations (39). Preliminary RIXS data show that the charge density changes during the $S_2$ to $S_3$ transition is much smaller than during the $S_1$ to $S_2$ transition, supporting the hypothesis that the oxidation is predominantly ligand-centered.

We think that the observed structural changes in the $S_2$ to $S_3$ transition are compatible with primarily a ligand centered oxidation. Oxidized ligand in the $S_3$ state can interconvert between a bridging or terminal ligand O atom (OH or $H_2O$) (40) resulting in a oxygen isotope exchange. Changes in Mn-O-Mn vibrational frequencies, the OEC EPR properties (11, 29), rate of water exchange (41) upon Ca to Sr substitution and data presented here indicate that the critical oxygen atom is part of the Mn-O-Ca/Sr bridging structure.

Although, there are many proposed mechanisms for the photosynthetic water oxidation reaction, that include variations on how the O-O bond is formed, there are two important favored mechanisms for water oxidation by the OEC that are: i) nucleophilic

attack on Mn(V)=O or Mn(IV)-O$^{\bullet}$ by metal (possibly Ca) bound water molecule or hydroxide (13, 42); or ii) reaction of a Mn-oxo unit with predominant radical character with an oxo/hydroxo/water ligand or an exogenous $H_2O$ (31). Except for PS II there are few structurally defined catalysts competent to oxidize water at room temperature; Ru- and Mn-complexes provide examples (42, 43). A theoretical investigation of the Ru catalyst supported a $Ru^{IV}$-O$^{\bullet}$ moiety to promote the water splitting reaction (44). Theoretical analysis of the OEC indicate that the formation of a low-lying ligand oxygen radical precursor state may be required for forming the O-O bond (39). To reach this state, a structural rearrangement is needed at the $S_2$ to $S_3$ transition. First, the changes in the Mn-Mn and Ca(Sr)-Mn distances require a model that involves a bridging oxygen atom, possibly the unique bridging $\mu_3$-oxygen atom (Fig. 4), which is probably the same oxygen where the oxidation occurs in the $S_3$ state, which triggers the formation of the O-O bond. Second, the decrease in the Ca(Sr)-Mn distance during the $S_2$ to $S_3$ transition favor the formation of the O-O bond between a Ca bound water or hydroxide and a Mn bound oxygen leading to the decrease in the Mn-Ca distances. These two observations lead us to propose that the Ca bound water or hydroxide and a critical oxo-bridging atom between the Mn atoms and Ca with predominant radical character are the oxygen atoms involved in the formation of the all-important O-O bond in the water oxidation reaction.

## Materials and Methods

**Sample preparation.** Sr-containing PS II (Sr-PS II) was prepared as described previously (29) with the exception that betaine concentration was decreased to 1 M. After elution from the Ni-affinity column, Sr-PS II was washed and concentrated using centrifugal filtration devices (Ultrafree-15, Millipore). Sr-PS II was finally resuspended

in 50 % glycerol, 1 M betaine, 15 mM $CaCl_2$, 15 mM $MgCl_2$, 40 mM Mes, pH 6.5 (adjusted with NaOH). Concentration of the Sr-PS II samples were ~15 mg Chl/ml.

EXAFS sample holders with inner dimension of 18 x 2.5 x 0.8 mm were filled with Sr-PS II samples. After dark-adaptation for 1 hour at room temperature, a freshly prepared stock solution (50 mM in ethanol) of phenyl-p-benzoquinone (PPBQ) was added to obtain a final concentration of 500 μM. PPBQ (Eastman Kodak) that was used these experiements was recrystallized several times from ethanol. All of the flash illumination, EPR, and x-ray absorption measurements were performed directly on samples mounted in these holders. The samples were immediately frozen to 77 K in liquid nitrogen after flash laser illumination.

**Metal Quantitation.** Metal (Mn and Sr) quantization was done using a Perkin Elmer 3110 Atomic Absorption Spectrometer equipped with an HGA 600 furnace. The quantitation yielded 37 ± 1 Chl / 4 Mn and 1.0 ± 0.1 Sr / 4 Mn.

**Flash-induced illumination of PS II.** A frequency-doubled (532 nm) Nd:YAG laser was used (8 ns pulse-width) for flash-illumination. In order to maintain maximal synchronization of the PS II centers upon flash illumination, fast recombination reaction between both the $S_2$ and $S_3$ states and the reduced form of the redox-active tyrosine residue $Y_D$ must be suppressed. This was achieved by the application of one preflash, followed by a 60 min dark adaptation period at room temperature. This procedure synchronizes the PS II centers into the $S_1Y_D^{ox}$ state. Each sample was then given 0, 1, 2, 3, 4, 5, 6 flashes at room temperature, with 1.5 s intervals between individual flashes. The light was focused on the sample using cylindrical lenses. After the last flash, the samples were frozen immediately (within 1 s) in liquid nitrogen. The EPR spectra were collected,

and the samples were stored at 77 K for further use in the XAS experiments. Additionally, $S_2$ samples were also prepared by 1 min continuous illumination at 200 K.

**Control with inactive Sr-PSII**. The *inactive* Sr-PSII was prepared by adding 10μL of a stock solution (100mM) of hydroxylamine ($NH_2OH$) directly to the intact Sr-PS II in the Lucite sample holder. After incubation for 20 min at room temperature in the dark, the sample was frozen in liquid nitrogen. $NH_2OH$ treated samples are indicated as HYD in the Figures.

**EPR spectroscopy**. Low-temperature X-band EPR spectra were recorded using a Varian E109 EPR spectrometer equipped with a model 102 microwave bridge. For the multiline signal measurements, the sample temperature was maintained at 8 K using an Air Products LTR liquid helium cryostat. Spectrometer conditions were as follows: microwave frequency, 9.21 GHz; field modulation amplitude, 32 G at 100 kHz; microwave power, 30 mW. EPR MLS amplitudes were quantified by adding peak-to-trough amplitudes of four of the upfield hyperfine lines (as indicated in Fig. S1A), relative to g=2. For each sample, the four designated $S_2$-state multiline EPR signal peaks were quantified by using the amplitude of the $Fe^{III}$ signal at g = 4.3 as a internal reference. The averaged results are shown as points in Figure S-1B, with the 1F value normalized to be 100%. Intensity of the MLS in the 1F samples and samples after continuous illumination were the same (within ±10% uncertainty of the quantitative EPR technique) ensuring the saturation of the sample with single laser flash illumination.

We have used the Kok model as in Messinger *et al*. (45) to calculate the S-state population for each flash number and have compared the normalized calculated $S_2$-state values (solid line, normalized to be 100% for 1F amplitude) to the normalized measured

amplitudes (squares) shown in Fig. S1B (Tables 3 and 4). The error between the calculated and measured $S_2$-states populations was minimized. Due to factors such as redox equilibrium between the cofactors in PS II, it is inevitable that some dephasing occurs while the OEC is advanced through the various S-states. The original Kok model explains this by assuming two parameters: the miss probability ($\alpha$) accounts for the percentage of centers that do not advance in each flash and the double-hit probability ($\beta$) describes the percentage of centers that make two turnovers in a single flash. The value of $\beta$ was first set to 0 based on the short pulse width of the Nd:YAG laser pulses. The possibility of double hits was considered in fit #2 and did not significantly improve the fit quality (Table 1). The low MLS intensity in the 5F sample could be due to insufficient statistics at this point or changes in the shape of the EPR MLS signal along the cycle or due to other, yet unknown, factors. Oscillation characteristics obtained by more precise $O_2$ evolution measurements or with UV absorption changes give comparable miss probability (29).

**EXAFS data collection**.

X-ray absorption spectra were collected at the Stanford Synchrotron Radiation Laboratory (SSRL) on beamline 9-3 at electron energy of 3.0 GeV and an average current of 70-100 mA. The intensity of the incident x-rays was monitored by a $N_2$-filled ion chamber ($I_0$) in front of the sample. The radiation was monochromatized by a Si(220) double-crystal monochromator. To reduce the sample damage by x-radiation, the incident x-ray beam was defocused at the sample position. The total photon flux on the sample was limited to 1 x $10^7$ photons per $\mu m^2$, which was determined to be non-damaging on the basis of detailed radiation damage studies of PS II solution samples (32). The samples

were protected from the beam during spectrometer movements between different energy positions by a shutter synchronized with the scan program. The samples were kept at 9 ± 1 K in a He atmosphere at ambient pressure using an Oxford CF-1208 continuous-flow liquid He cryostat. Data were recorded as fluorescence excitation spectra using a germanium 30-element energy-resolving detector (Canberra Electronics). For Mn XAS energy was calibrated by the pre-edge peak of $KMnO_4$ (6543.3 eV), which was placed between two $N_2$-filled ionization chambers ($I_1$ and $I_2$) after the sample.

Conditions for acquiring Sr EXAFS data on *Thermosynechococcus elongatus* Sr-PS II samples closely resemble those for spinach solution and oriented samples and described in Cinco *et al*. (17, 19). The x-ray flux at 16-17 keV was between 2 and $5x10^9$ photons $s^{-1}mm^{-2}$ of sample. For energy calibration, we simultaneously measured the absorption spectrum of solid strontium acetate, whose edge peak was assigned the value 16120.0 eV. Spectra were collected with 3eV steps in the pre-edge region (15970-16070 eV), 1 eV steps from 16070 to 16134 eV, and 0.075 $Å^{-1}$ steps from $k$=2.0-13.5 $Å^{-1}$. Sr EXAFS data were recorded during 3 beam times for $S_1$ and $S_2$ and $S_3$ samples and during two beam times for $S_0$ samples resulting in identical spectra from different protein preparations.

This work was supported by the NIH Grant GM 55302, and by the Director, Office of Science, Office of Basic Energy Sciences (OBES), Division of Chemical Sciences, Geosciences, and Biosciences of the Department of Energy (DOE) under Contract DE-AC02-05CH11231. We thank M. Sugiura and A. W. Rutherford for continuing scientific discussions and J. Messinger, C. F. Yocum and G. C. Dismukes for discussions about the role of Ca. Synchrotron facilities were provided by the Stanford

Synchrotron Radiation Laboratory (SSRL) operated by DOE OBES. The SSRL Biomedical Technology program is supported by NIH, the National Center for Research Resources, and the DOE Office of Biological and Environmental Research.

**References**


1. Ort, D. R. & Yocum, C. F. (1996) *Oxygenic Photosynthesis; The Light Reactions.* (Kluwer Academic Publishers, Dordrecht, The Netherlands).
2. Wydrzynski, T. & Satoh, S. (2005) *Photosystem II: The Light-Driven Water:Plastoquinone Oxidoreductase* (Springer, Dordrecht, The Netherlands).
3. Britt, R. D. (1996) in *Oxygenic Photosynthesis: The Light Reactions*, eds. Ort, D. R. & Yocum, C. F. (Kluwer Academic Publishers, Dordrecht, The Netherlands), pp. 137-164.
4. Peloquin, J. M. & Britt, R. D. (2001) *Biochim. Biophys. Acta* **1503,** 96-111.
5. Carrell, T. G., Tyryshkin, A. M. & Dismukes, G. C. (2002) *J. Biol. Inorg. Chem.* **7,** 2-22.
6. Charlot, M.-F., Boussac, A. & Blondin, G. (2005) *Biochim. Biophys. Acta* **1708,** 120-132.
7. Hasegawa, K., Ono, T.-A., Inoue, Y. & Kusunoki, M. (1999) *Chem. Phys. Lett.* **300,** 9-19.
8. Yachandra, V. K., Sauer, K. & Klein, M. P. (1996) *Chem. Rev.* **96,** 2927-2950.
9. Yachandra, V. K. (2002) *Philos. Trans. R. Soc. Lond. Ser. B-Biol. Sci.* **357,** 1347-1357.
10. Sauer, K. & Yachandra, V. K. (2004) *Biochim. Biophys. Acta* **1655,** 140-148.
11. Chu, H.-A., Hillier, W., Law, N. A. & Babcock, G. T. (2001) *Biochim. Biophys. Acta* **1503,** 69-82.
12. Debus, R. J., Strickler, M. A., Walker, L. M. & Hillier, W. (2005) *Biochemistry* **44,** 1367-1374.

13. Ferreira, K. N., Iverson, T. M., Maghlaoui, K., Barber, J. & Iwata, S. (2004) *Science* **303,** 1831-1838.

14. Loll, B., Kern, J., Saenger, W., Zouni, A. & Biesiadka, J. (2005) *Nature* **438,** 1040-1044

15. Latimer, M. J., DeRose, V. J., Mukerji, I., Yachandra, V. K., Sauer, K. & Klein, M. P. (1995) *Biochemistry* **34,** 10898-10909.

16. Latimer, M. J., DeRose, V. J., Yachandra, V. K., Sauer, K. & Klein, M. P. (1998) *J. Phys. Chem. B* **102,** 8257-8265.

17. Cinco, R. M., Robblee, J. H., Rompel, A., Fernandez, C., Yachandra, V. K., Sauer, K. & Klein, M. P. (1998) *J. Phys. Chem. B* **102,** 8248-8256.

18. Cinco, R. M., Holman, K. L. M., Robblee, J. H., Yano, J., Pizarro, S. A., Bellacchio, E., Sauer, K. & Yachandra, V. K. (2002) *Biochemistry* **41,** 12928-12933.

19. Cinco, R. M., Robblee, J. H., Messinger, J., Fernandez, C., Holman, K. L. M., Sauer, K. & Yachandra, V. K. (2004) *Biochemistry* **43,** 13271-13282.

20. Yano, J., Pushkar, Y., Glatzel, P., Lewis, A., Sauer, K., Messinger, J., Bergmann, U. & Yachandra, V. K. (2005) *J. Am. Chem. Soc.* **127,** 14974-14975.

21. Yano, J., Kern, J., Sauer, K., Latimer, M., Pushkar, Y., Biesiadka, J., Loll, B., Saenger, W., Messinger, J., Zouni, A. & Yachandra, V. K. (2006) *Science* **314,** 821-825.

22. Boussac, A. & Rutherford, A. W. (1988) *Biochemistry* **27,** 3476-3483.

23. Vrettos, J. S., Stone, D. A. & Brudvig, G. W. (2001) *Biochemistry* **40,** 7937-7945.

24. Westphal, K. L., Lydakis-Simantiris, N., Cukier, R. I. & Babcock, G. T. (2000) **39,** 16220-16229.

25. Britt, R. D., Campbell, K. A., Peloquin, J. M., Gilchrist, M. L., Aznar, C. P., Dicus, M. M., Robblee, J. & Messinger, J. (2004) *Biochim. Biophys. Acta-Bioenergetics* **1655,** 158-171.

26. Chu, H.-A., Sackett, H. & Babcock, G. T. (2000) *Biochemistry* **39,** 14371-14376.

27. Kimura, Y., Hasegawa, K. & Ono, T. (2002) *Biochemistry* **41,** 5844-5853.

28. Strickler, M. A., Walker, L. M., Hillier, W. & Debus, R. J. (2005) *Biochemistry* **44,** 8571-8577.

29. Boussac, A., Rappaport, F., Carrier, P., Verbavatz, J. M., Gobin, R., Kirilovsky, D., Rutherford, A. W. & Sugiura, M. (2004) *J. Biol. Chem.* **279,** 22809-22819.

30. Messinger, J., Robblee, J. H., Bergmann, U., Fernandez, C., Glatzel, P., Visser, H., Cinco, R. M., McFarlane, K. L., Bellacchio, E., Pizarro, S. A., Cramer, S. P., Sauer, K., Klein, M. P. & Yachandra, V. K. (2001) *J. Am. Chem. Soc.* **123,** 7804-7820.

31. Liang, W., Roelofs, T. A., Cinco, R. M., Rompel, A., Latimer, M. J., Yu, W. O., Sauer, K., Klein, M. P. & Yachandra, V. K. (2000) *J. Am. Chem. Soc.* **122,** 3399-3412.

32. Yano, J., Kern, J., Irrgang, K.-D., Latimer, M. J., Bergmann, U., Glatzel, P., Pushkar, Y., Biesiadka, J., Loll, B., Sauer, K., Messinger, J., Zouni, A. & Yachandra, V. K. (2005) *Proc. Natl. Acad. Sci. USA* **102,** 12047-12052.

33. Mishra, A., Yano, J., Pushkar, Y., Yachandra, V. K., Abboud, K. A. & Christou, G. (2007) *Chem. Comm.* **15,** 1538-1540.

34. Kuntzleman, T., McCarrick, M., Penner-Hahn, J. & Yocum, C. (2004) *Phys. Chem. Chem. Phys.* **6,** 4897-4904.

35. Pushkar, Y., Yano, J., Glatzel, P., Messinger, J., Lewis, A., Sauer, K., Bergmann, U. & Yachandra, V. K. (2006) *J. Biol. Chem.* **282,** 7198-7208.

36. Boussac, A. & Rutherford, A. W. (1988) *FEBS Lett.* **236,** 432-436.

37. Chu, H. A., Hillier, W. & Debus, R. J. (2004) *Biochemistry* **43,** 3152-3166.

38. Kimura, Y., Mizusawa, N., Yamanari, T., Ishii, A. & Ono, T. (2005) *J. Biol. Chem.* **280,** 2078-2083.

39. Siegbahn, P. E. M. & Crabtree, R. H. (1999) *J. Amer. Chem. Soc.* **121,** 117-127.

40. McEvoy, J. P. & Brudvig, G. W. (2006) **106,** 4455-4483.

41. Hendry, G. & Wydrzynski, T. (2003) *Biochemistry* **42,** 6209-6217.

42. Vrettos, J. S., Limburg, J. & Brudvig, G. W. (2001) *Biochim. Biophys. Acta* **1503,** 229-245.

43. Yamada, H., Siems, W. F., Koike, T. & Hurst, J. K. (2004) *J. Am. Chem. Soc.* **126,** 9786-9795.

44. Yang, X. & Baik, M.-H. (2006) *J. Am. Chem. Soc.* **128,** 7476-7485.

45. Messinger, J., Robblee, J. H., Bergmann, U., Fernandez, C., Glatzel, P., Visser, H., Cinco, R. M., McFarlane, K. L., Bellacchio, E., Pizarro, S. A., Cramer, S. P., Sauer, K., Klein, M. P. & Yachandra, V. K. (2001) *J. Am. Chem. Soc.* **123,** 7804-7820.

**Table 1: Fits to the $S_2$ Multiline EPR Signal Oscillation Pattern**

| Fit N | α, % | β, % | Fit error | Fit quality |
|---|---|---|---|---|
| 1 | 13.0 | 0 | 38 | 6.3 |
| 2 | 12.9 | 1.0 | 28 | 5.6 |

The fit error and fit quality were calculated as following: Fit error = $\Sigma(\text{residual}^2)$ and fit quality = (fit error)/(7-number of free parameters) (45).

**Table 2: S-state Composition of Samples Given 0 to 3 Flashes**

| Number of Flashes | $S_0$ | $S_1$ | $S_2$ | $S_3$ |
|---|---|---|---|---|
| 0F | 0.0 | 100.0 | 0.0 | 0.0 |
| 1F | 0.0 | 13.0 | 87.0 | 0.0 |
| 2F | 0.0 | 1.7 | 22.6 | 75.7 |
| 3F | 65.9 | 0.2 | 4.4 | 29.5 |

**Table 3: One- and Two-Shell Simulations of Mn EXAFS Fourier Peak II from the $S_1$, $S_2$, $S_3$ and $S_0$ States.**

| Fit N | Sample | Shell | $R$ (Å) | $N$ (with $S_0^2$=0.85) | $\sigma^2$(Å$^2$)x10$^3$ | $\Delta E_0$ | $\Phi$(x10$^3$) | $\varepsilon^2$(x10$^5$) |
|---|---|---|---|---|---|---|---|---|
| One Shell | | | | | | | | |
| 1 | $S_1$ | Mn-Mn | 2.73 | 1.08 | 1.7 | -16 | 0.20 | 0.10 |
| 2 | $S_2$ | Mn-Mn | 2.74 | 1.13 | 1.6 | -15 | 0.22 | 0.10 |
| 3 | $S_3$ | Mn-Mn | 2.76 | 1.35 | 3.3 | -14 | 0.31 | 0.15 |
| 4 | $S_0$ | Mn-Mn | 2.73 | 1.26 | 2.0 | -16 | 0.30 | 0.16 |
| Two Shells | | | | | | | | |
| 5 | $S_3$ | Mn-Mn<br>Mn-Mn | 2.75<br>2.88 | 1.13<br>0.45 | 1* | -11 | 0.23 | 0.11 |
| 6 | $S_0$ | Mn-Mn<br>Mn-Mn | 2.73<br>2.85 | 1.14<br>0.25 | 1* | -15 | 0.28 | 0.14 |

*parameter was fixed.

The high-resolution EXAFS method can distinguish two distances 2.7 and 2.8 Å contributing to peak II in the $S_1$ and $S_2$ states (20, 35). However, conventional EXAFS has less resolving power, and peak II in $S_1$ and $S_2$ states is fit with one shell of Mn-Mn interactions. The increased Debye-Waller factor for the one-shell fit of the $S_3$ state favors the two-shell fit.

**Table 4: Two-Shell Simulations of Fourier Peak II (Sr-Mn distances) from the $S_1$, $S_2$, $S_3$ and $S_0$ states.**

| Fit | S-state | Shell | *R* (Å) | **N* (Sr-Mn Interactions) | $\sigma^2$(Å$^2$)x10$^3$ | $\Phi$(x10$^3$) | $\varepsilon^2$(x10$^5$) |
|---|---|---|---|---|---|---|---|
| 1 | $S_1$ | Sr-Mn | 3.53 | 3 | 7.0 | 0.45 | 0.18 |
| | | Sr-Mn | 4.02 | 1 | 7.0 | | |
| 2 | $S_1$ | Sr-Mn | 3.52 | 2 | 5.5 | 0.62 | 0.25 |
| | | Sr-Mn | 3.99 | 2 | 5.5 | | |
| 3 | $S_1$ | Sr-Mn | 3.52 | 2 | 4.6 | 0.58 | 0.24 |
| | | Sr-Mn | 3.99 | 1 | 4.6 | | |
| 1 | $S_2$ | Sr-Mn | 3.51 | 2 | 7.7 | 0.37 | 0.15 |
| | | Sr-Mn | 3.97 | 2 | 7.7 | | |
| 2 | $S_2$ | Sr-Mn | 3.56 | 3 | 9.6 | 0.48 | 0.19 |
| | | Sr-Mn | 4.03 | 1 | 9.6 | | |
| 1 | $S_3$ | Sr-Mn | 3.42 | 2 | 8.9 | 0.56 | 0.23 |
| | | Sr-Mn | 3.94 | 2 | 8.9 | | |
| 1 | $S_0$ | Sr-Mn | 3.47 | 2 | 6.8 | 0.23 | 0.10 |
| | | Sr-Mn | 3.98 | 2 | 6.8 | | |

*R* is the distance between Sr and Mn. **N* the number of Sr-Mn Interactions was fixed at values of 0, 1, 2, 3 and 4. $\sigma$ is the Debye-Waller factor. $\Phi$ and $\varepsilon^2$ are the goodness-of-fit parameters. Details about parameters and fitting methodology are described in the supplementary material and Fig. S3.

Figure Captions

Fig. 1 (A) Mn K-edge XANES spectra of Sr-PS II from *Thermosynechococcus elongatus* (top), and the corresponding second derivatives of the XANES spectra (bottom) in the $S_1$, $S_2$, $S_3$ and $S_0$ states. The inflection point of the edges and the shape of the spectra are clearly different between the S-states. (B) Fourier transforms of $k^3$-weighted Mn EXAFS (Fig. S2) of Sr-PS II in the different S-states ($S_1$, $S_2$, $S_3$, $S_0$). The detailed fit parameters of the Mn EXAFS spectra are included in Tables 3 and S1-S2.

**Fig. 2 (A)** Sr K-edge XANES spectra of Sr-PS II from *Thermosynechococcus elongatus* (top), and the corresponding second derivatives of the XANES spectra (bottom) in the $S_1$, $S_2$, $S_3$ and $S_0$ states and an *inactive* control sample (HYD). The inflection point of the edges and the shape of the spectra are clearly different between the control and the intermediate S-states. There are small but distinct differences in the S-state spectra which are easier to see in the second derivatives (bottom). The two dashed lines indicate the clear systematic differences in the Sr K-edge spectra between the S-states; peak labeled a shifts to higher energy and peak b shifts to lower energy as we advance from $S_0$ through $S_3$ states. Other small differences are also seen in the second derivatives. **(B)** Fourier transforms of $k^3$-weighted Sr EXAFS (Fig. S3) of Sr-PS II in the different S-states ($S_1$, $S_2$, $S_3$, $S_0$), and an *inactive* control sample prepared by hydroxylamine treatment of Sr-PS II. The dominant Fourier peak I is due to ligating oxygens in the first coordination sphere to Sr. Peak II is best fit by four Sr-Mn interactions; two short distances at ~3.5 and two longer Sr-Mn distances at ~4.0 Å. FT peak II from Sr-Mn is dependent on the particular S-state and shows that structure of cluster changes as we advance through the S-states,

with a significant change occurring between the critical $S_2$ to $S_3$ transition suggesting that the cluster is flexible and this might be important for the function. The control sample only shows the FT peak from Sr-O backscattering, because the cluster is disrupted and thereby the Sr-Mn interactions. The detailed fit parameters of the Sr EXAFS spectra are included in Tables 4 and S3-S5.

**Fig. 3 (A)** Ca atom (in green) and Sr atom (in yellow) were placed into the structural model derived from a polarized Mn EXAFS experiment on PS II single crystals (model II)(21) in the $S_1$ state. The number of the Sr-Mn vectors and the Sr-Mn distances are from the results of fits to Sr EXAFS data (Fit 1 in Table 4); (Sr-$Mn_{B,C,D}$ at ~3.5 Å and Sr-$Mn_A$ at ~4.0 Å). Only small changes in the Sr atom position are required, compared to the position of the Ca determined from polarized EXAFS studies of PS II crystals, to satisfy the Sr EXAFS data from Sr-PS II. **(B)** The Fourier transforms of the Sr-EXAFS spectra from Sr-PS II of the $S_1$ state calculated using *ab initio* FEFF8 program for the placement of the Sr atom that is in accord with the best fit number 1 in Table 4. Coordinates of Model II(21) with Sr as in Fit 1 Table 4, were used as input. Figure shows that peak II in the Sr EXAFS spectrum of PS II originates from Sr-Mn interaction. There is very good agreement between the experimental FTs from the Sr EXAFS spectra from Sr-PS II with the calculated FT for the Model.

**Fig. 4** Schematic of the structural changes accompanying the S-state transitions in the $Mn_4Ca(Sr)$ cluster is placed within the context of the recent structural model from single-crystal x-ray spectroscopy. The critical transition is the $S_2$ to $S_3$ advancement, when the

Mn-Mn di-μ-oxo bridge distances of the $Mn_4$-core become elongated from ~2.7-2.8 Å to ~2.8-2.9 Å. Simultaneously, Sr is drawn closer to the Mn core with the Sr-Mn interaction at ~3.5 Å shortening to ~3.4 Å and at ~4.0 Å distance decreasing to 3.94 Å. We propose that this significant change is triggered by the ligand centered oxidation of the oxygen atom that bridges the Mn with the Ca atoms. The proposed Ca(Sr)-Mn distances in all the S-states are indicated in the boxes next to the S-states. The critical bridging oxygen atom is show in blue. The dashed line between Ca and the bridging atom in the $S_2$ state indicates the possible movement of Ca closer towards two of the Mn atoms. The four dashed lines in the $S_3$ state indicate a change in the structure around the $\mu_3$-oxo bridged oxygen, probably from a tetrahedral to tetragonal distortion and leading to the changes in the Mn-Mn and Ca(Sr)-Mn distances.

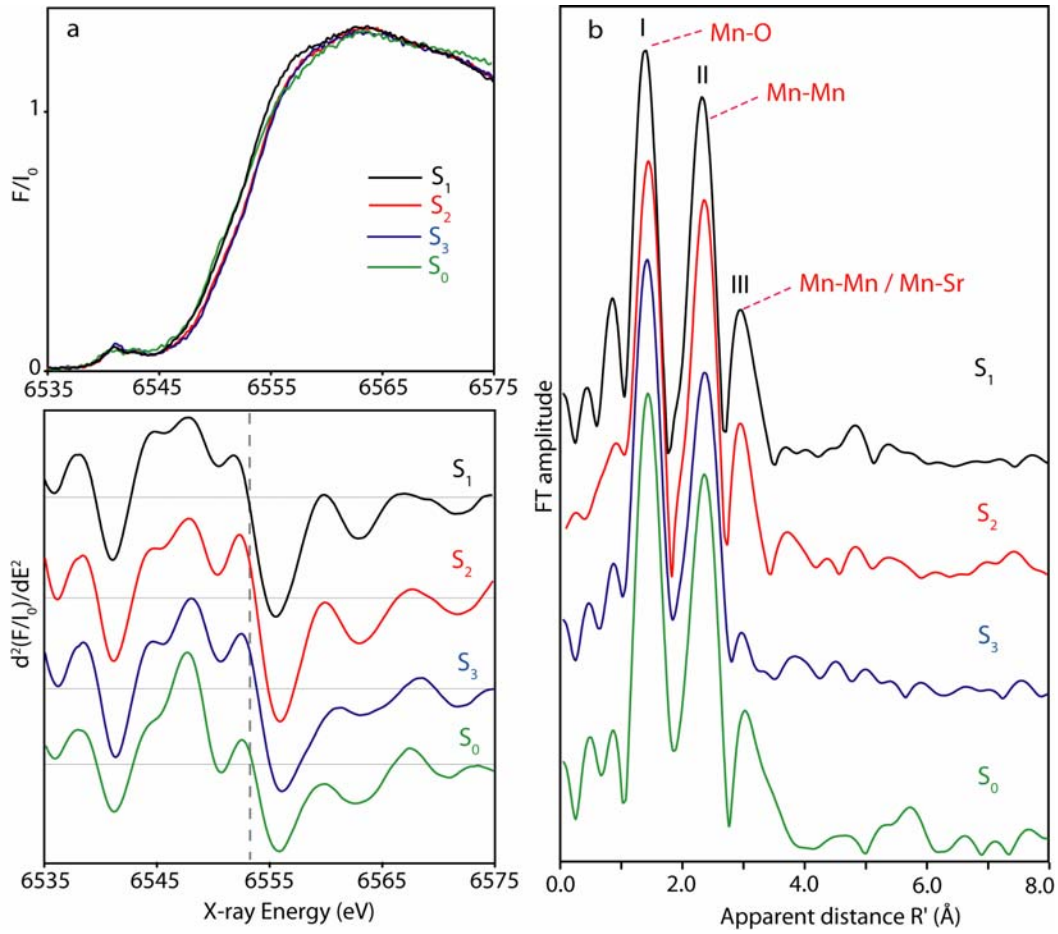
a
1
0
F/I0
S1
S2
S3
S0
6535
6545
6555
6565
6575
d2(F/I0)/dE2
X-ray Energy (eV)
b
I
Mn-O
II
Mn-Mn
III
Mn-Mn / Mn-Sr
FT amplitude
0.0
2.0
4.0
6.0
8.0
Apparent distance R' (Å)

Figure 1

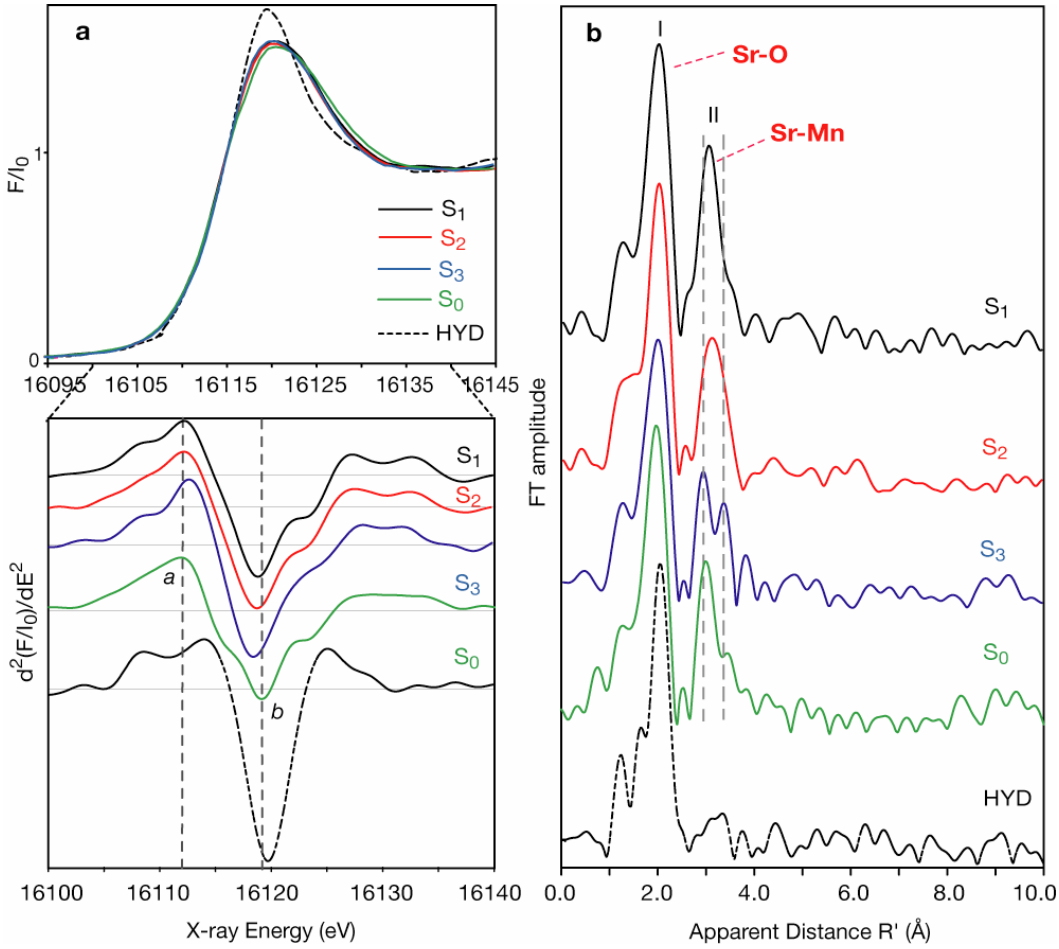
a
F/I0
1
0
16095
16105
16115
16125
16135
16145
S1
S2
S3
S0
HYD
d2(F/I0)/dE2
a
b
16100
16110
16120
16130
16140
X-ray Energy (eV)
b
I
II
Sr-O
Sr-Mn
FT amplitude
S1
S2
S3
S0
HYD
0.0
2.0
4.0
6.0
8.0
10.0
Apparent Distance R' (Å)

Figure 2

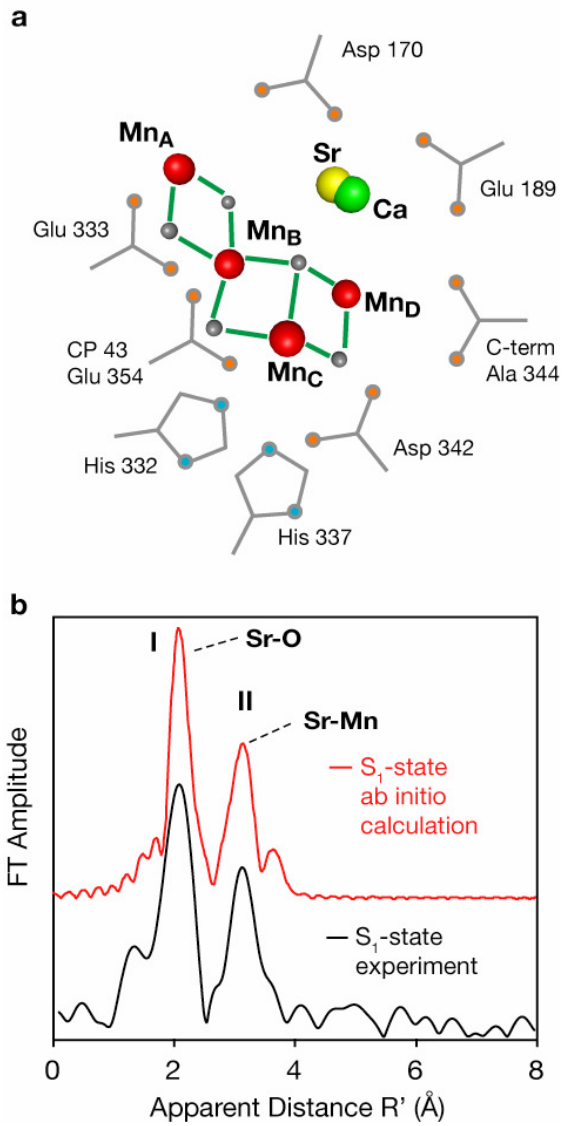
a
Asp 170
Mn_A
Sr
Ca
Glu 189
Glu 333
Mn_B
Mn_D
CP 43
Glu 354
Mn_C
C-term
Ala 344
His 332
Asp 342
His 337
b
I
Sr-O
II
Sr-Mn
— S1-state
ab initio
calculation
— S1-state
experiment
FT Amplitude
0
2
4
6
8
Apparent Distance R' (Å)

Figure 3

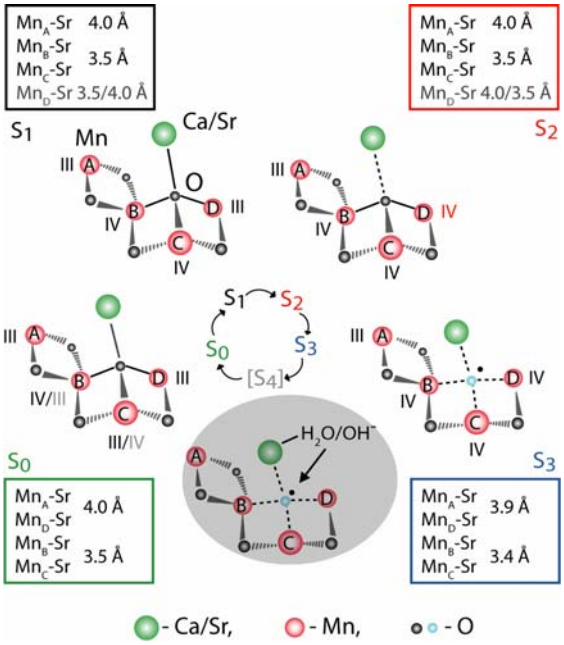
Mn_A-Sr 4.0 Å
Mn_B-Sr 3.5 Å
Mn_C-Sr
Mn_D-Sr 3.5/4.0 Å
S1
Mn
Ca/Sr
O
Mn_A-Sr 4.0 Å
Mn_B-Sr 3.5 Å
Mn_C-Sr
Mn_D-Sr 4.0/3.5 Å
S2
S1
S2
S0
S3
[S4]
IV/III
III/IV
S0
Mn_A-Sr 4.0 Å
Mn_D-Sr
Mn_B-Sr 3.5 Å
Mn_C-Sr
H2O/OH-
S3
Mn_A-Sr 3.9 Å
Mn_D-Sr
Mn_B-Sr 3.4 Å
Mn_C-Sr
- Ca/Sr,
- Mn,
- O

Figure 4